Astroparticle Physics 34 (2011) 521–527

Contents lists available at ScienceDirect

Astroparticle Physics

journal homepage: www.elsevier.com/locate/astropart

Performance of the Virgo interferometer longitudinal control system during the second science run

T. Accadia [u], F. Acernese [f,h], F. Antonucci [n], P. Astone [n], G. Ballardin [b], F. Barone [f,h], M. Barsuglia [a], A. Basti [k,l], Th.S. Bauer [w], M.G. Beker [w], A. Belletoile [u], S. Birindelli [y], M. Bitossi [k], M.A. Bizouard [s], M. Blom [w], F. Bondu [z], L. Bonelli [k,l], R. Bonnand [v], V. Boschi [k], L. Bosi [i], B. Bouhou [a], S. Braccini [k], C. Bradaschia [k], A. Brillet [y], V. Brisson [s], R. Budzyński [af], T. Bulik [ag,ah], H.J. Bulten [w,x], D. Buskulic [u], C. Buy [a], G. Cagnoli [c], E. Calloni [f,g], E. Campagna [c,d], B. Canuel [b], F. Carbognani [b], F. Cavalier [s], R. Cavalieri [b], G. Cella [k], E. Cesarini [d], O. Chaibi [y], E. Chassande-Mottin [a], A. Chincarini [e], F. Cleva [y], E. Coccia [p,q], C.N. Colacino [k,l], J. Colas [b], A. Colla [n,o], M. Colombini [o], A. Corsi [n], J.-P. Coulon [y], E. Cuoco [b], S. D'Antonio [p], V. Dattilo [b], M. Davier [s], R. Day [b], R. De Rosa [f,g], G. Debreczeni [al], M. del Prete [k,m], L. Di Fiore [f], A. Di Lieto [k,l], M. Di Paolo Emilio [p,r], A. Di Virgilio [k], A. Dietz [u], M. Drago [ac,ad], V. Fafone [p,q], I. Ferrante [k,l], F. Fidecaro [k,l], I. Fiori [b], R. Flaminio [v], L.A. Forte [f], J.-D. Fournier [y], J. Franc [v], S. Frasca [n,o], F. Frasconi [k], A. Freise [am], M. Galimberti [v], L. Gammaitoni [i,j], F. Garufi [f,g], M.E. Gáspár [al], G. Gemme [e], E. Genin [b], A. Gennai [k], A. Giazotto [k], R. Gouaty [u], M. Granata [a], C. Greverie [y], G.M. Guidi [c,d], J.-F. Hayau [z], H. Heitmann [y,z], P. Hello [s], S. Hild [an], D. Huet [b], P. Jaranowski [ai], I. Kowalska [ag], A. Królak [ae,aj], N. Leroy [s], N. Letendre [u], T.G.F. Li [w], N. Liguori [aa,ab], M. Lorenzini [c], V. Loriette [t], G. Losurdo [c], E. Majorana [n], I. Maksimovic [t], N. Man [y], M. Mantovani [k,m], F. Marchesoni [i], F. Marion [u], J. Marque [b], F. Martelli [c,d], A. Masserot [u], C. Michel [v], L. Milano [f,g], Y. Minenkov [p], M. Mohan [b], N. Morgado [v], A. Morgia [p,q], S. Mosca [f,g], V. Moscatelli [n], B. Mours [u], I. Neri [i,j], F. Nocera [b], G. Pagliaroli [p,r], L. Palladino [p,r], C. Palomba [n], F. Paoletti [k,b], S. Pardi [f,g], M. Parisi [g], A. Pasqualetti [b], R. Passaquieti [k,l], D. Passuello [k], G. Persichetti [f,g], M. Pichot [y], F. Piergiovanni [c,d], M. Pietka [ai], L. Pinard [v], R. Poggiani [k,l], M. Prato [e], G.A. Prodi [aa,ab], M. Punturo [i], P. Puppo [n], D.S. Rabeling [w,x], I. Rácz [al], P. Rapagnani [n,o], V. Re [aa,ab], T. Regimbau [y], F. Ricci [n,o], F. Robinet [s], A. Rocchi [p], L. Rolland [u], R. Romano [f,h], D. Rosińska [ak], P. Ruggi [b], B. Sassolas [v], D. Sentenac [b], L. Sperandio [p,q], R. Sturani [c,d], B. Swinkels [b], A. Toncelli [k,l], M. Tonelli [k,l], O. Torre [k,m], E. Tournefier [u], F. Travasso [i,j], G. Vajente [k,l,*], J.F.J. van den Brand [w,x], S. van der Putten [w], M. Vasuth [al], M. Vavoulidis [s], G. Vedovato [ac], D. Verkindt [u], F. Vetrano [c,d], A. Viceré [c,d], J.-Y. Vinet [y], H. Vocca [i], R.L. Ward [a], M. Was [i], M. Yvert [u]

[a] Laboratoire AstroParticule et Cosmologie (APC), Université Paris Diderot, CNRS: IN2P3, CEA: DSM/IRFU, Observatoire de Paris 10, rue A. Domon et L. Duquet, 75013 Paris, France
[b] European Gravitational Observatory (EGO), I-56021 Cascina (PI), Italy
[c] INFN, Sezione di Firenze, I-50019 Sesto Fiorentino, Italy
[d] Università degli Studi di Urbino 'Carlo Bo', I-61029 Urbino, Italy
[e] INFN, Sezione di Genova, I-16146 Genova, Italy
[f] INFN, Sezione di Napoli, Complesso Universitario di Monte S. Angelo, I-80126 Napoli, Italy
[g] Università di Napoli 'Federico II', Complesso Universitario di Monte S. Angelo, I-80126 Napoli, Italy
[h] Università di Salerno, Fisciano, I-84084 Salerno, Italy
[i] INFN, Sezione di Perugia, I-06123 Perugia, Italy
[j] Università di Perugia, I-06123 Perugia, Italy
[k] INFN, Sezione di Pisa, I-56127 Pisa, Italy
[l] Università di Pisa, I-56127 Pisa, Italy
[m] Università di Siena, I-53100 Siena, Italy
[n] INFN, Sezione di Roma, I-00185 Roma, Italy
[o] Università 'La Sapienza', I-00185 Roma, Italy
[p] INFN, Sezione di Roma Tor Vergata, I-00133 Roma, Italy
[q] Università di Roma Tor Vergata, I-00133 Roma, Italy
[r] Università dell'Aquila, I-67100 L'Aquila, Italy
[s] LAL, Université Paris-Sud, IN2P3/CNRS, F-91898 Orsay, France
[t] ESPCI, CNRS, F-75005 Paris, France
[u] Laboratoire d'Annecy-le-Vieux de Physique des Particules (LAPP), Université de Savoie, CNRS: IN2P3, F-74941 Annecy-Le-Vieux, France
[v] Laboratoire des Matériaux Avancés (LMA), IN2P3/CNRS, F-69622 Villeurbanne, Lyon, France
[w] Nikhef, National Institute for Subatomic Physics, P.O. Box 41882, 1009 DB Amsterdam, The Netherlands
[x] VU University Amsterdam, De Boelelaan 1081, 1081 HV Amsterdam, The Netherlands

doi:10.1016/j.astropartphys.2010.11.006

[y] Université Nice-Sophia-Antipolis, CNRS, Observatoire de la Côte d'Azur, F-06304 Nice, France
[z] Institut de Physique de Rennes, CNRS, Université de Rennes 1, 35042 Rennes, France
[aa] INFN, Gruppo Collegato di Trento, I-38050 Povo, Trento, Italy
[ab] Università di Trento, I-38050 Povo, Trento, Italy
[ac] INFN, Sezione di Padova, I-35131 Padova, Italy
[ad] Università di Padova, I-35131 Padova, Italy
[ae] IM-PAN, 00-956 Warsaw, Poland
[af] Warsaw University, 00-681 Warsaw, Poland
[ag] Astronomical Observatory, Warsaw University, 00-478 Warsaw, Poland
[ah] CAMK-PAN, 00-716 Warsaw, Poland
[ai] Białystok University, 15-424 Białystok, Poland
[aj] IPJ, 05-400 Świerk-Otwock, Poland
[ak] Institute of Astronomy, 65-265 Zielona Góra, Poland
[al] RMKI, H-1121 Budapest, Konkoly Thege Miklós út 29-33, Hungary
[am] University of Birmingham, Birmingham B15 2TT, United Kingdom
[an] University of Glasgow, Glasgow G12 8QQ, United Kingdom

ARTICLE INFO

Article history:
Received 28 June 2010
Received in revised form 23 September 2010
Accepted 24 November 2010
Available online 4 December 2010

ABSTRACT

The second science run of the Virgo gravitational wave interferometer took place between July 2009 and January 2010. This paper describes the performance of the interferometer longitudinal control system in terms of duty cycle, stability and control noise. A science data taking duty cycle of about 80% was obtained over the six month run. Control noise was not limiting the detector sensitivity at any frequency. A discussion of observed thermal effects in the detector operation is also included.

1. Introduction

The Virgo gravitational wave detector [1], located at the EGO site near Pisa in Italy, is a power-recycled Michelson interferometer with 3 km long Fabry–Perot resonant cavities in the two arms. Any gravitational signal will be detected as a differential change of optical length of the arms proportional to the signal amplitude $h \sim \delta L/L$. All mirrors are suspended to high-performance multistage passive isolation systems (the *super-attenuators* [2]) designed to filter the transmission of ground micro-seismic vibration to the test masses. These ensure a good sensitivity to gravitational waves down to 10 Hz. The input laser beam is provided by a 60 W Nd:YAG laser amplifier with a wavelength of 1.064 μm. Before entering the main part of the interferometer, the beam passes through an *input mode cleaner* (IMC) to filter its transverse mode and reduce jitter. A schematic of the Virgo detector is shown in Fig. 1.

With respect to the first science run VSR1 [4], the laser input power injected into the interferometer was doubled to 17 W. Thermal lensing due to laser power absorption in the input mirror substrates needed to be corrected by a thermal compensation system (TCS) [6].

The second Virgo detector Science Run (VSR2) started on July 7th 2009 and ended six months later on January 8th 2010. During that period the Virgo interferometer collected data in a controlled and stable way, partly in coincidence with the two LIGO detectors [3] located in the USA.

The detector stability was remarkably high, allowing a total science data duty cycle of about 80%, see Fig. 2. The main limitations on duty cycle were periodic maintenance, scheduled commissioning activities, and the time needed to bring the interferometer to science mode from an uncontrolled state (about 30 min). The longest continuous lock of the instrument lasted about 143 h.

This paper describes the performance of the longitudinal control system during VSR2. It therefore updates and extends what is reported in the previous paper [4] which referred to VSR1 and later commissioning periods. A more detailed description of the longitudinal control scheme can be found in the cited paper [4].

2. Longitudinal control system

In order to maintain the correct resonance condition inside the interferometer and the best possible detector sensitivity, distances between mirrors must be controlled by active feed-back systems with typical accuracy better than 10^{-12} m. The longitudinal control system is also called the *locking system* and it deals with four main degrees of freedom: the differential change in length of the two Fabry–Perot arm cavities (DARM) which corresponds to the main degree of freedom sensitive to the effect of a gravitational wave signal; the mean change in length of the two cavities (CARM) which is also equivalent to a change in the main laser frequency; the length of the power recycling cavity (PRCL) composed of the power recycling mirror and the two arm input mirrors; the differential change in length of the two short Michelson arms (MICH) between beam splitter and the two input mirrors. All these degrees of freedom are controlled using digital feed-back systems with typical band-widths of 1–50 Hz and actuated using coil-magnet pairs at the level of the mirrors, with the only exception of CARM. For this degree of freedom the control strategy is two-fold. A fast control is done acting on the laser frequency, which follows the average length of the two arms with large band-width (about 10 kHz). This is implemented using an analog control system as larger band-width is needed. In addition a slow (1 Hz) mechanical control is done stabilizing CARM against a rigid reference cavity (RFC) to remove large common-mode motions of the two cavities. For more details refer to Section 2 of [4] or [7].

The main laser beam is phase modulated at radio-frequency (about 6 MHz) and the four degrees of freedom are controlled using different optical error signals, coming from demodulation of photo-diode outputs both in-phase and quadrature (frontal modulation scheme, see also Section 2 of [4,5]). In the *steady-state* condition (operation at maximum sensitivity) the control strategy chosen during VSR2 was the following: the dark port in-phase signal (B1) was used to control DARM, while the quadrature for MICH; the beam-splitter pick-off beam (B5) in-phase signal was used for

* Corresponding author at: INFN, Sezione di Pisa, I-56127 Pisa, Italy. Tel.: +39 050752354.
E-mail address: gabriele.vajente@sns.it (G. Vajente).

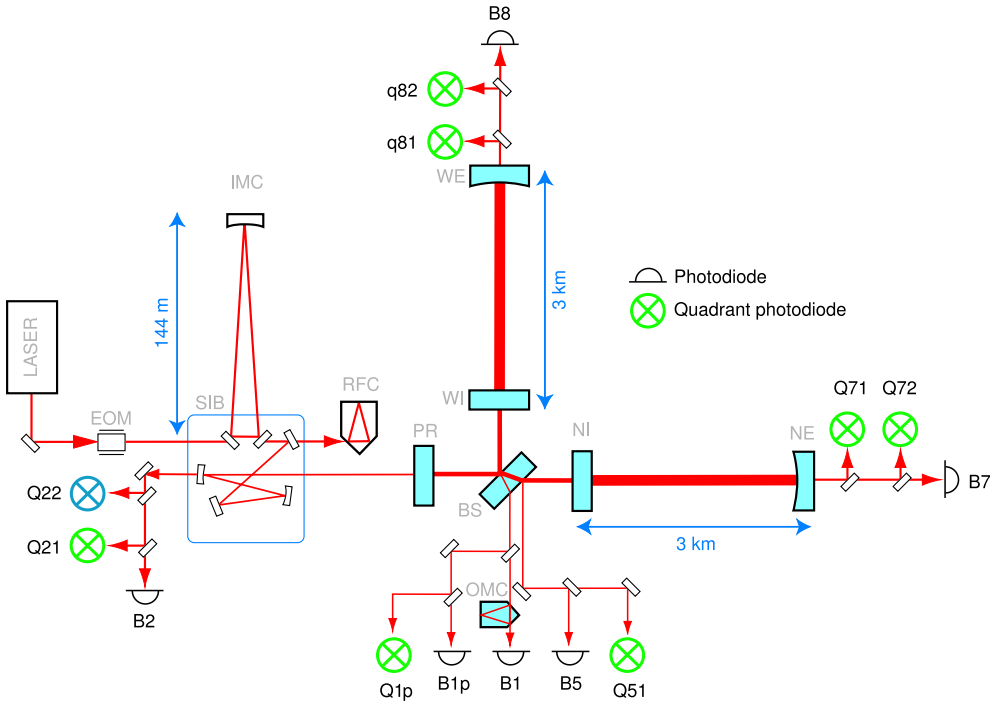

Fig. 1. Optical schematic of the Virgo interferometer. Main output beams: B1 is the anti-symmetric port, B2 is the interferometer reflection, B5 is the pick-off beam from the secondary face of the beam splitter, B7 and B8 are the transmission of the two arm Fabry–Perot cavities. The two end mirror (NE and WE) high reflection surfaces have a mean radius of curvature of about 3500 m. The two input mirrors (NI and WI) have all flat surfaces.

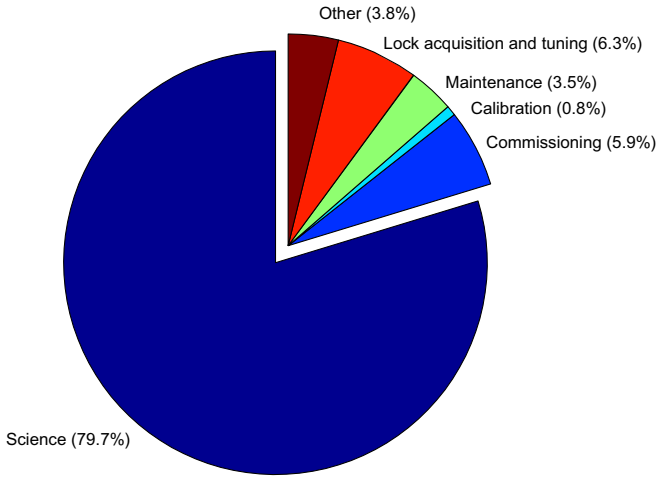

Fig. 2. Science mode duty cycle of the Virgo detector during the second science run (VSR2).

laser frequency stabilization and the quadrature signal for PRCL; the reference cavity (RFC) in-phase signal was used for the narrow bandwidth CARM control. A global reconstruction of low-frequency arm cavity length variations from DARM and CARM corrections were used for feed-back control of the upper stage of the super-attenuators, independent of ground bases sensors. This strategy is based on the fact that at frequencies below few hundreds mHz the control system gains are very high and therefore the correction signals follow exactly the degree of freedom motion, making it possible to use them as displacement sensors.

With respect to VSR1 [4], different ports were used for the reconstruction of the central interferometer longitudinal degrees of freedom (MICH and PRCL). Indeed the new signals are not significantly different in term of shot noise, but are less affected by other technical disturbances, like scattered light. Moreover, using this control strategy, both quadratures of B1 and B5 are maintained close to zero with a feed-back loop, reducing local oscillator phase noise in the signals (see Section 7.8 of [7]).

Fig. 3 shows the typical spectra and total RMS of the four longitudinal degrees of freedom residual motions during steady state operations. The total RMS residual displacements are: 8×10^{-16} m for DARM, 2×10^{-13} m for PRCL, 3×10^{-12} m for MICH and 9×10^{-9} m for CARM. These are much improved with respect to VSR1 (see Table 1 and Table 1 of [4]), mainly due to better performance of the automatic alignment system, improved error signals, and increased gains of the longitudinal control system at low frequency.

3. Thermal effects and thermal compensation system

The lock acquisition procedure is responsible for bringing the interferometer from a completely uncontrolled state to the steady state condition. In Virgo this procedure is carried out by passing through several intermediate steps in which the interferometer can be stably operated (*variable finesse technique* [8]). Initially each arm cavity is locked independently, the power recycling mirror slightly misaligned and MICH locked with an offset to be at gray (50%) fringe. In a second step the power recycling mirror is realigned and its cavity brought in resonance. Finally the offset is adiabatically removed to reach the steady-state condition which corresponds to the maximum power build up inside the arm cavities. In this condition about 13 kW circulate inside the Fabry–Perot arms.

Having reached the steady state condition, the power absorbed in the input mirror coatings becomes not negligible. The heat absorbed by the coating is transferred by conduction to the mirror substrate, creating there a temperature gradient which reproduces the laser beam central Gaussian profile. Two kind of thermal effects are present: thermo-elastic deformation of the mirror high

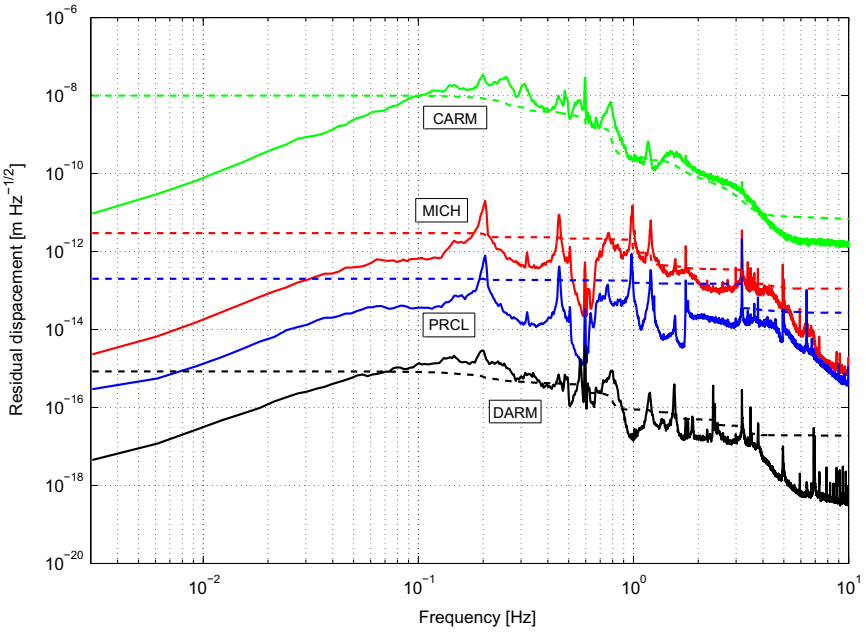

Fig. 3. Residual displacements of all longitudinal degrees of freedom in steady state conditions. Solid curves show the spectrum of the residual motion, dashed curves the integrated RMS.

reflecting surface, which is negligible; thermo-optical change in index of refraction which is dominant and produces a converging thermal lens in the mirror substrate. At first order this lens has no effect on the carrier field, since it is resonant inside the Fabry–Perot cavities and cleaned by them. Instead the thermal lens disturbs the sideband mode-matching to the power recycling cavity. Their recycling gain is reduced and the spatial content is aberrated. Both aberration and recycling gain reduction have a negative effect on the ability to extract longitudinal degrees of freedom from photo-diode signals.

In VSR1 the input power was limited to 8 W in order to maintain these thermal effect at a sustainable level. In order to surpass this limit and improve sideband recycling gain, a thermal compensation system (TCS) [6] was installed in Virgo between VSR1 and VSR2. This system projects an annulus of 10 micron laser light, obtained by shaping auxiliary CO_2 lasers, onto the front face of each input mirror, heating the area external to the main interferometer beam and thus creating a diverging lens to compensate the central converging one. The TCS laser is always shined on the input mirrors, even when the interferometer is not locked, to avoid large temperature transients at switch on and off. During VSR2, thermal lensing in the input mirrors was only partially compensated to obtain residual aberrations at the level of VSR1, using about 1 W of CO_2 power for each input mirror.[1] The estimated residual lens had a focal length of the order of 15 km [9].

Fig. 4 shows the typical carrier and sideband recycling gains evolution in time, after reaching dark fringe during VSR2. The carrier gain is estimated from the total power on the B5 beam while the sideband gain is monitored demodulating the same diode at twice the modulation frequency. During an initial transient sideband gain is temporarily maximum. However as the input mirrors achieve thermal equilibrium (in about 15 min) the gain is reduced by half. Fig. 5 shows the sideband and carrier spatial contents during the transient and at thermal equilibrium, detected using a *phase camera* [10] placed at the dark port before the output mode cleaner. The sidebands thermally induced aberration is very clear from the plots of Fig. 5.

Table 1
Requirements and obtained performance of the longitudinal control loops in terms of residual total RMS motion of the main degrees of freedom.

D.O.F.	Requirements [m]	Accuracy [m]	
		VSR1	VSR2
DARM	$3 \cdot 10^{-11}$	$3 \cdot 10^{-12}$	$8 \cdot 10^{-16}$
PRCL	$2 \cdot 10^{-10}$	$3 \cdot 10^{-11}$	$2 \cdot 10^{-13}$
MICH	$5 \cdot 10^{-10}$	$8 \cdot 10^{-11}$	$3 \cdot 10^{-12}$
CARM		$4 \cdot 10^{-8}$	$9 \cdot 10^{-9}$

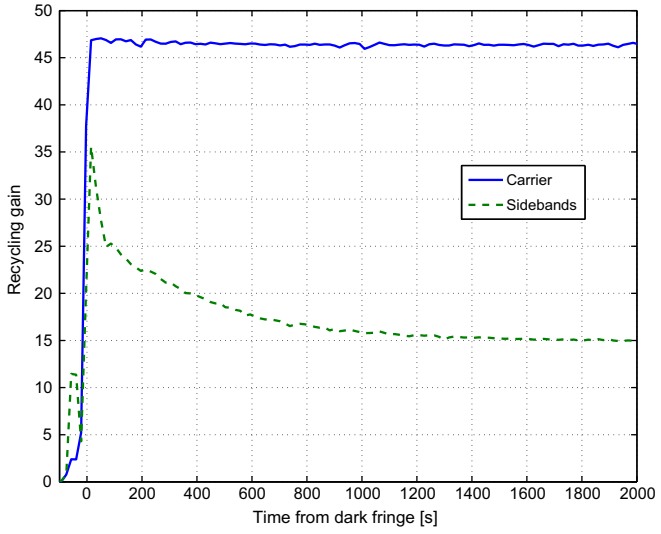

Fig. 4. Evolution of carrier and sideband recycling gain with time during the thermal transient that follows the reaching of the maximum power build up in the arm cavities. Carrier recycling gain is constant around 47, while the sideband one start from a maximum of about 37 and settles down to about 15. Maximum values are compatible with what is expected from simulations.

[1] The maximum usable TCS power was limited by the fact that the CO_2 lasers were not yet intensity stabilized. Increasing the amount of TCS power would have introduced intensity noise in the main gravitational channel.

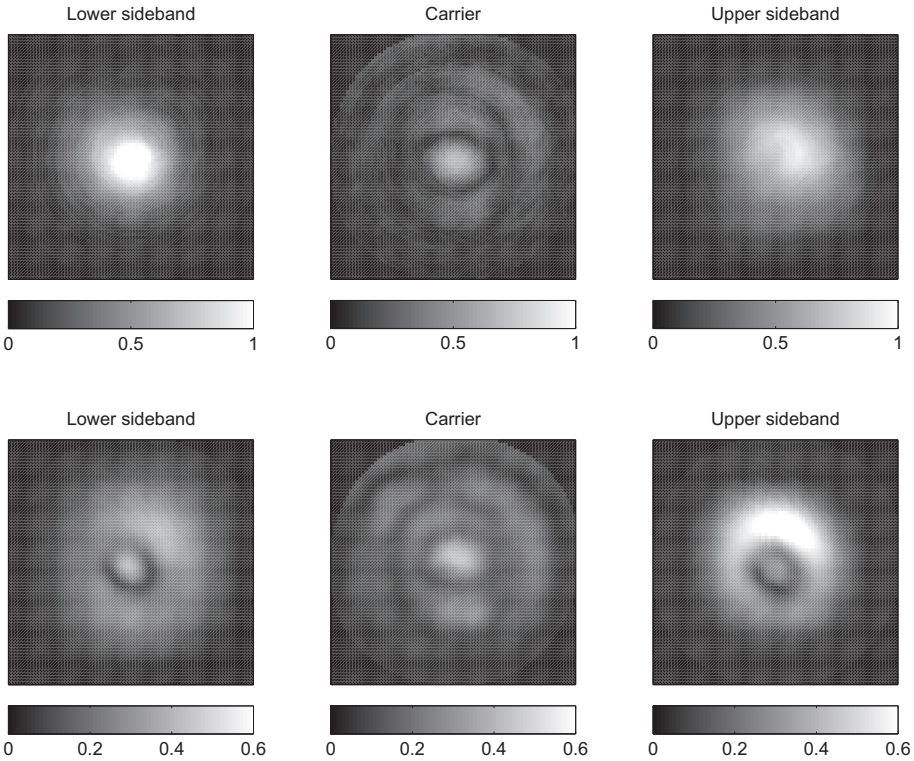

Fig. 5. Amplitude images of fields at dark port (before the output mode cleaner), obtained using the phase camera. The top plots show the situation immediately after reaching the maximum power build up in the arm cavities. Sidebands have a reasonably good shape. The TCS correction is always applied (even when the interferometer is unlocked) and consequently the two input mirrors have a negative curvature at the beginning of the lock. Since the amount of TCS power is different for the two mirrors, the different shape of the two sidebands is explained. The bottom plots shows the steady state condition. The sideband shapes are very far from the Gaussian one expected if thermal effects were well compensated. Carrier images show the high order mode content due to interferometer asymmetries.

The overlap integral between the carrier and sideband fields at dark port is:

$$S = \frac{\left|\int\int \psi^*_{CAR}(x,y)\psi_{SB}(x,y)\,\mathrm{d}x\,\mathrm{d}y\right|}{\sqrt{\int\int |\psi_{CAR}(x,y)|^2\,\mathrm{d}x\,\mathrm{d}y}\sqrt{\int\int |\psi_{SB}(x,y)|^2\,\mathrm{d}x\,\mathrm{d}y}}. \quad (1)$$

The largest possible optical gain is obtained when this quantity is one and the two fields overlap perfectly. The integral in the numerator involves the knowledge of the phase of the fields, which was not available. However an upper limit can be obtained using the field amplitudes only since:

$$\left|\int\int \psi^*_{CAR}(x,y)\psi_{SB}(x,y)\,\mathrm{d}x\,\mathrm{d}y\right| \leqslant \int\int |\psi_{CAR}(x,y)||\psi_{SB}(x,y)|\,\mathrm{d}x\,\mathrm{d}y. \quad (2)$$

In the steady-state condition the carrier field at dark port is dominated by junk contributions originating from interferometer defects and cannot be used as an estimate of ψ_{CAR}. Therefore we obtain this estimate adding an offset in the MICH locking point such that the dark port carrier field is dominated by the pure mode resonating inside the power recycling cavity. This temporary configuration have been used for the measurement purpose only. Sideband field instead is always dominated by the contribution originated from the Schnupp asymmetry and therefore ψ_{SB} is easily measured in steady state condition.

For VSR2 the overlap integrals between sideband and carrier are estimated to be smaller than 0.2 (upper sideband) and 0.25 (lower sideband) at the end of the thermal transient, while at the beginning they are estimated to be smaller than 0.6 and 0.7. These values are not unity since the TCS correction is always applied to the mirrors, even with the interferometer not locked. This means that at the beginning of the thermal transient the input mirrors are over-corrected, resulting in smaller-than-unity overlap integral.

4. Noise couplings to gravitational channel

The feed-back loops that control the auxiliary degrees of freedom are limited by sensing noise above 10 Hz. This noise is typically not of a fundamental nature (like shot-noise for example) but coming from other technical sources like scattered light [11] or electronic noise. The contribution of this spurious coupling mechanisms to the detector sensitivity can be directly estimated by means of projection measurements, as already explained in Section 4 of [4]. Fig. 6 shows the typical results obtained during VSR2. All auxiliary longitudinal control noises were more than a factor 10 lower than the measured sensitivity at all frequencies.

As explained in Section 4 of [4] some improvements in control noise reduction were already obtained immediately after the end of the first run. The main actions was the use of signal from different interferometer ports as explained in Section 2, obtaining higher signal to noise ratio. Nevertheless the sensor noise of these signals would be limiting the sensitivity up to few hundreds hertz if no noise subtraction technique is used. These were already implemented during the first run [4] and consisted in feeding the DARM correction with filtered auxiliary channel corrections in such a way to exactly cancel the direct optical coupling. The efficiency of these techniques relies on the accuracy of the measurement of coupling transfer functions and of the fitting technique used. Between VSR1 and VSR2 the measurement accuracy improved thanks to the overall reduction of detector noise and to the use of colored noise to optimally distribute the perturbation energy. The fitting accuracy significantly improved using a more powerful algorithm [12].

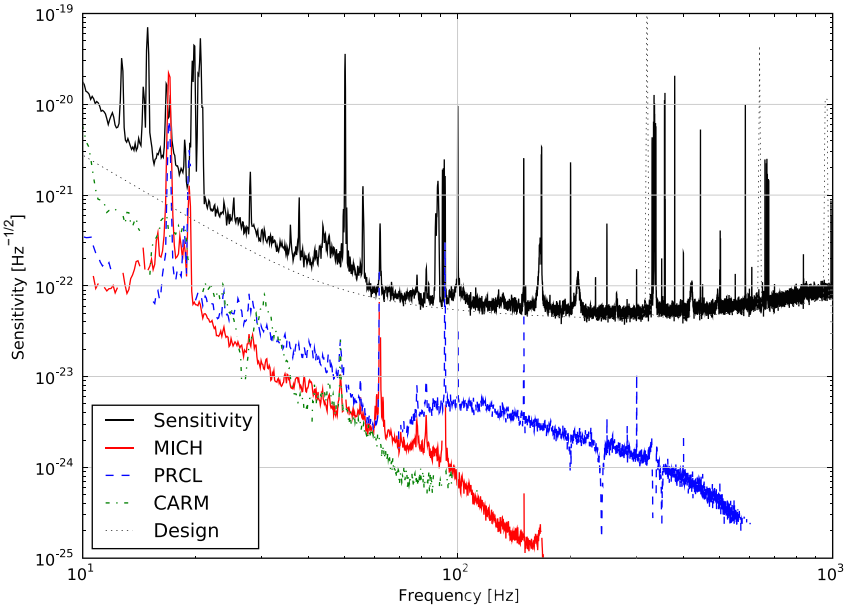

Fig. 6. Typical measured contribution of longitudinal control noise to the Virgo detector sensitivity during VSR2. The projected noise is below the design sensitivity at all frequencies and safely far from the measured one. 11 and 62 Hz peaks are calibration lines added on purpose.

In summary, with respect to [4] the situation further improved mainly due to the final change of central interferometer degrees of freedom reconstruction strategy explained in Section 2 and the reduction of noise contributions coming from scattered light. With respect to the best configuration shown in [4], control noise contribution has been reduced at all frequencies a factor 10 below design sensitivity.

The largest contribution, even if not limiting the measured sensitivity, is the one coming from the CARM control system. Investigations are on-going to characterize and reduce the sensor noise, which seems mainly affected by non-linear up conversion due to beam jitter in front of the RFC.

5. Conclusions

During VSR2, the Virgo interferometer ran with high input power (17 W) and with a thermal compensation system which, though not yet optimally tuned, allowed great robustness and stability (science mode duty cycle almost at 80%). Residual aberration of radio-frequency sidebands have been estimated in two ways. An upper limit of the sideband recycling gain is measured to be 15, about 2.5 times lower than the maximum one which is observed at the beginning of the lock acquisition, when thermal effects are not yet large. A phase camera has been used to show that the sideband shape is far from being Gaussian and the superposition with the carrier is estimated to be smaller than 0.25.

The control accuracy was improved with respect to VSR1 [4], even if already compliant with requirements. Finally the re-introduced control noise was a safe factor 10 below the measured detector sensitivity at all frequency, further improving the situation described in [4].

The coming upgrade of Virgo foresee the use of fused silica fibers to suspend the test masses, in order to reduce the suspension thermal noise. Moreover the cavity finesse will increase from 50 to 150. Assuming the same level of sensing noise will be measured in the longitudinal error signal, MICH and PRCL coupling will decrease with the increase of finesse, being at the level of the improved design sensitivity. Excluding CARM control that will need some improvements (better noise subtraction, reduction of sensor noise, reduced control band-width) the present longitudinal control strategy is already compliant with the target sensitivity of the next Virgo science run (after the installation of fused silica mirror suspension fibers) and with the expected sensitivity of Advanced Virgo detector.

Acknowledgements

The authors gratefully acknowledge the support of the Italian Istituto Nazionale di Fisica Nucleare and the French Centre National de la Recherche Scientifique for the construction and operation of the Virgo detector.

The authors also gratefully acknowledge the support of the research by the Foundation for Fundamental Research on Matter of the Netherlands Organization for Scientific Research, the Polish Ministry of Science and Higher Education Grant No. N203 387237, the FOCUS Programme of Foundation for Polish Science and the European Associated Laboratory Astrophysics Poland–France.

The work has been carried out also with support of the Italian Ministero dell'Istruzione, dell'Universita' e della Ricerca through grant PRIN 2007NXMBHP.

References

[1] F. Acernese et al., Virgo Collaboration, Status of Virgo, in: Proceeding of the 7th Amaldi Conference, published in Classical Quantum Gravity, vol. 25, 2008, p. 114045.
[2] F. Acernese et al., Virgo Collaboration, Measurements of superattenuator seismic isolation by Virgo interferometer, Astropart. Phys. 33 (2010) 182–189.
[3] J.R. Smith et al., LIGO Scientific Collaboration, The path to the enhanced and advanced LIGO gravitational-wave detectors, Classical Quantum Gravity 26 (2009) 114013.
[4] F. Acernese et al., Virgo Collaboration, Performances of the Virgo interferometer longitudinal control system, Astropart. Phys. 33 (2010) 75–80.
[5] R.W. Drever, J.L. Hall, F.V. Kowalski, J. Hough, G.M. Ford, A.J. Munley, H. Ward, Laser phase and frequency stabilization using an optical resonator, Appl. Phys. B 97 (1983) 31.
[6] T. Accadia et al., Virgo Collaboration, A thermal compensation system for the gravitational wave detector Virgo, in: Proceedings of 12th Marcel Grossmann Meeting, Link to conference talk material <www.icra.it/MG/mg12/talks/gw2_dipaolo.pdf>.

[7] G. Vajente, Analysis of Sensitivity and Noise Sources for the Virgo Gravitational Wave Interferometer, Ph.D. Thesis, Scuola Normale Superiore di Pisa, 2008. Available from: <https://tds.ego-gw.it/ql/?c=7469>.
[8] F. Acernese et al., Virgo Collaboration, The variable finesse locking technique, Classical Quantum Gravity 23 (2006) S85.
[9] R. Day, V. Fafone, J. Marque, M. Pichot, M. Punturo, A. Rocchi, Virgo Input Mirrors Thermal Effects Characterization, Virgo Internal Document VIR-0191A-10. Available from: <https://tds.ego-gw.it/ql/?c=7325>.
[10] R. Day, Multi-field wave-front sensor for measuring thermal effects in a gravitational wave detector, in: 8th Amaldi Conference. Available from: <http://sites.google.com/site/amaldi8project/presentations/4Day.pdf?attredirects=0&d=1>.
[11] T. Accadia et al., Virgo Collaboration, Noise from scattered light in Virgo's second science run data, Classical Quantum Gravity 27 (2010) 194011.
[12] B. Gustavsen, A. Semlyen, Rational approximation of frequency domain responses by vector fitting, IEEE Trans. Power Delivery 14 (3) (1999) 1052–1061.